SPACE SCIENCES

Long-lasting, deep effect of Saturn's giant storms

Cheng Li[1]*, Imke de Pater[2,3], Chris Moeckel[3], R. J. Sault[4], Bryan Butler[5], David deBoer[2], Zhimeng Zhang[6]

Planetary-scale giant storms erupt on Saturn quasiperiodically. There have been at least six recorded occurrences of past eruptions, and the most recent one was in 2010, with its whole life span captured by the Cassini mission. In 2015, we used the Very Large Array to probe the deep response of Saturn's troposphere to the giant storms. In addition to the remnant effect of the storm in 2010, we have found long-lasting signatures of all mid-latitude giant storms, a mixture of equatorial storms up to hundreds of years old, and potentially an unreported older storm at 70°N. We derive an ammonia anomaly map that shows an extended meridional migration of the storm's aftermath and vertical transport of ammonia vapor by storm dynamics. Intriguingly, the last storm in 2010 splits into two distinct components that propagate in opposite meridional directions, leaving a gap at 43°N planetographic latitude.

INTRODUCTION

Every 20 to 30 years, a giant storm erupts on Saturn, creating enormous cloud disturbances with a clear head marching forward until it wraps around the whole planet (*1*, *2*). The most recent eruption was in 2010, with visible cloud activities lasting for more than 6 months (*3*–*5*). At that time, the Cassini spacecraft was still orbiting Saturn and the on-board instruments, including the visible camera, radio instruments, infrared camera [composite infrared spectrometer (CIRS)], and Cassini Radar, returned exquisite details of the astronomical feast. The next event is expected to happen within 10 to 20 years, based on prior statistics and the understanding of the storm dynamics (*1*, *2*, *6*). In the stratosphere, more than 10 K temperature anomalies appeared in a concentrated stratospheric beacon and lasted for 2 to 3 years after the storm (*7*, *8*), causing a substantial change in the chemical composition in a local area (*9*, *10*).

Despite similarities between the giant planets, storms of these sizes are unique to Saturn. One peculiar aspect of the last giant storm on Saturn is its "dehydration" effect, referring to the observation that the storm depletes the condensable vapors in the atmosphere, in particular, the ammonia vapor. Since ammonia vapor provides sufficient microwave opacity at the altitudes probed by the Cassini/Radar instrument, the observed high brightness temperatures in the Cassini Radar's radiometric observation at 2 cm was interpreted as being caused by a completely dry atmosphere, i.e., no ammonia vapor, down to at least ~2 bar (*11*, *12*).

This observation was puzzling because moist convection would bring ammonia-rich air from deep levels to shallower levels, which should enrich the ammonia vapor concentration in the shallower layers rather than deplete it. The apparent contradiction can be explained by the interstorm meridional circulation. Unlike dry convection, moist convection is asymmetric with respect to updrafts and downdrafts: The initial updrafts carry moist and saturated air upward, but the subsequent downdrafts push dry and unsaturated air downward. The process may oscillate several times, leaving behind an overall unsaturated atmosphere (*6*). Similar arguments have been used to explain a depletion of ammonia on Jupiter in the upper versus lower atmospheric layers (*13*).

Another possible mechanism to remove ammonia vapor is by forming ammonia-rich mushballs (*14*, *15*). Protected by a thin ice shell, ammonia-rich (up to 30%) liquid (*16*) can be sealed within centimeter-sized hail-like precipitation and be effectively transported to the deep atmosphere. Sequestration of ammonia vapor into a cold ammonia-water solution at shallower layers and release of it at deep layers where the temperature is high may explain the depletion of ammonia gas. This mechanism also indicates colder but ammonia-rich deep layers due to evaporation. A warm and dry upper layer sitting on top of a cold and moist deep layer stabilizes the atmosphere and prevents the occurrence of moist convection for many years. However, the post-storm stable stratification would be eroded away by the infrared cooling of the atmosphere and by turbulent mixing that homogenizes the ammonia concentration. Both processes are slow because the cooling flux is low and the atmosphere is nearly inviscid.

We examine the long-term evolution of the atmosphere of Saturn after the 2010 storm using the upgraded Karl G. Jansky Very Large Array (VLA). No big storms were observed after the last giant eruption, and the post-storm evolution of the atmosphere would be governed by the aforementioned slow process: infrared cooling and mixing. Saturn's atmosphere is a huge heat reservoir, even for the shallow part at altitudes above the 30-bar pressure level. Using the emitted power, 5 W/m^2, 5 years of cooling will only lead to a change in the column-averaged temperature by about 0.2 K (*17*). Thus, we suspect that observed variations in brightness temperature, while sensitive to both temperature and ammonia variations, are predominantly due to variations in the ammonia vapor.

RESULTS

VLA observations

VLA observations of Saturn were obtained on two dates: 24 to 25 January 2015 when the array was in its compact configuration

[1]Climate and Space Sciences and Engineering, University of Michigan, Ann Arbor, MI, USA. [2]Department of Astronomy, University of California, Berkeley, Berkeley, CA, USA. [3]Department of Earth and Planetary Science, University of California, Berkeley, Berkeley, CA, USA. [4]School of Physics, University of Melbourne, Victoria 3010, Australia. [5]National Radio Astronomy Observatory, Socorro, NM, USA. [6]Geological and Planetary Sciences, California Institute of Technology, Pasadena, CA, USA.
*Corresponding author. Email: chengcli@umich.edu.

(C&B), and 28 to 29 May 2015 with the array in its more extended configuration (B&A). These are hybrid configurations in which the antennas on the east and west arms have already been moved to the more compact configuration, but those on the north arm remain extended. Such array configurations are ideal to observe sources at relatively low declinations. In January (C&B), the planet was observed in the Q (39.8 to 47.6 GHz), K (18 to 26 GHz), U (12 to 17 GHz), and X bands (8 to 11.8 GHz), and in May (B&A) in S (2 to 2.5 GHz), C (4 to 4.2 GHz), X (8 to 11.2 GHz), and U (12 to 17 GHz) bands.

These data were presented previously in the analysis of Saturn's ring system (*18*), with a summary of observations provided in their table 1. All data were initially processed and calibrated using the internal VLA calibration pipeline, followed by using the MIRIAD software to self-calibrate, clean, and map the data (*19*). On the basis of a preliminary model fitting of Saturn's disk (*18*), we determined the disk-averaged brightness temperatures in each band, as summarized in table S1.

Figure 1 shows current and previous observations of Saturn's disk-averaged radio emission, together with a model spectrum for comparison. This disk-averaged model assumes a dry adiabatic atmosphere and a uniform distribution of ammonia vapor up to the cloud base, referred to as the homogeneous isentropic model. Above the cloud base, the ammonia vapor follows its saturation value uniquely determined by the temperature. We use the Voyager radio occultation profile (*20*) for temperatures at altitudes above the 1-bar pressure level and use an adiabatic extrapolation for temperatures below the 1-bar level. The VLA channels do not probe deep enough to see through the condensation level of water, so we used a nominal value of 10 times the solar water abundance (*21*), estimated from the dynamics of Saturn's giant storm (*6*). The disk-averaged brightness temperatures of the C and S bands are sensitive to the ammonia concentration above the water cloud level near 20 bars. The χ^2 fitting of both bands reduces to $\chi^2 < 1$ for an ammonia abundance of around 200 parts per million by volume (ppmv), which corresponds to an enrichment factor of 1.5 compared to the solar N abundance (see the Supplementary Materials, section A, for a study on the ammonia concentration). However, this value may not be truly representative of Saturn's deep ammonia abundance because the S band is not long enough to distinguish various deep ammonia abundances [see the comparison of two other models using 150 and 400 ppm deep ammonia abundance (*22*, *23*)]. Nonetheless, Saturn's disk-averaged emission can be fitted adequately by a homogeneous isentropic model, while Jupiter's atmosphere shows substantial depletion of ammonia vapor in the upper layers compared to the deep atmosphere (*24*–*26*).

Figure 2 shows images of Saturn in different projections for all six radio bands with the ring contribution removed. The left column displays residual disk images as viewed on the sky with a limb-darkened disk subtracted (based on disk-averaged parameters as shown in table S1); the middle column projects the residual disk image into a cylindrical projection, with rotational smearing of about 60° in longitude; the right column zooms in on the polar region northward of 50°N. We obtain the limb of the disk by tracing the sharp edge of the full disk image and overlaying that on the residual disk image. We focus our analysis on the northern hemisphere where the line of sight was free of ring materials.

Clear signatures of bright and dark latitudinal bands are found from the residual disk images at wavelengths shorter than 10 cm (C, X, U, K, and Q bands). At the S band, the banded structure is barely visible except for the shadow of Saturn's ring in the southern hemisphere. However, this may be due to the low spatial resolution of the S-band image (~10° in latitude). The C-band image starts to show one bright latitudinal band between 20°N and 40°N and a relatively

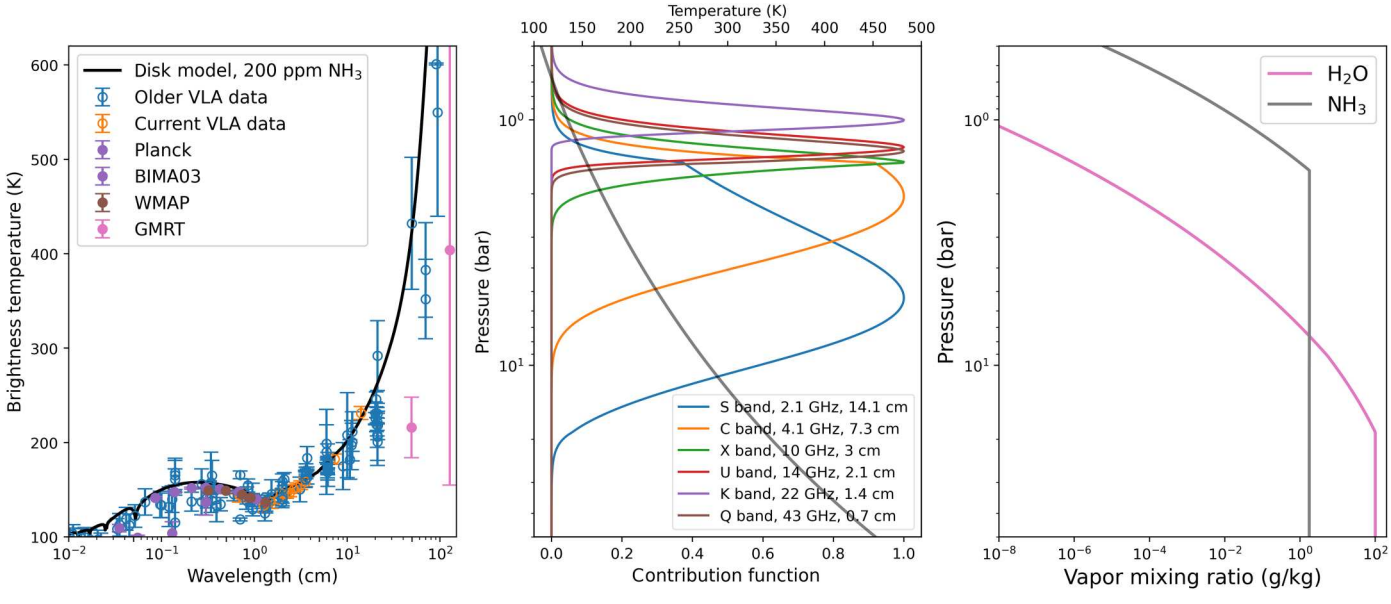

Fig. 1. Disk-averaged observation and model of Saturn. (**Left**) Saturn's disk-averaged brightness temperature as a function of wavelength. VLA observations from this paper are shown by the orange points. The blue dots are older data (*22*, *38*, *42*–*44*). Wilkinson microwave anisotropy probe (WMAP) (*45*) and Planck (*46*, *47*) data are shown in chocolate and magenta colors, respectively. All data have been corrected for cosmic microwave background radiation, and use the full Planck equation (rather than the Rayleigh-Jeans approximation) to convert flux densities to brightness temperatures. (**Middle**) Contribution function of the radio bands and the dry adiabatic temperature profile. (**Right**) Ammonia and water profiles.

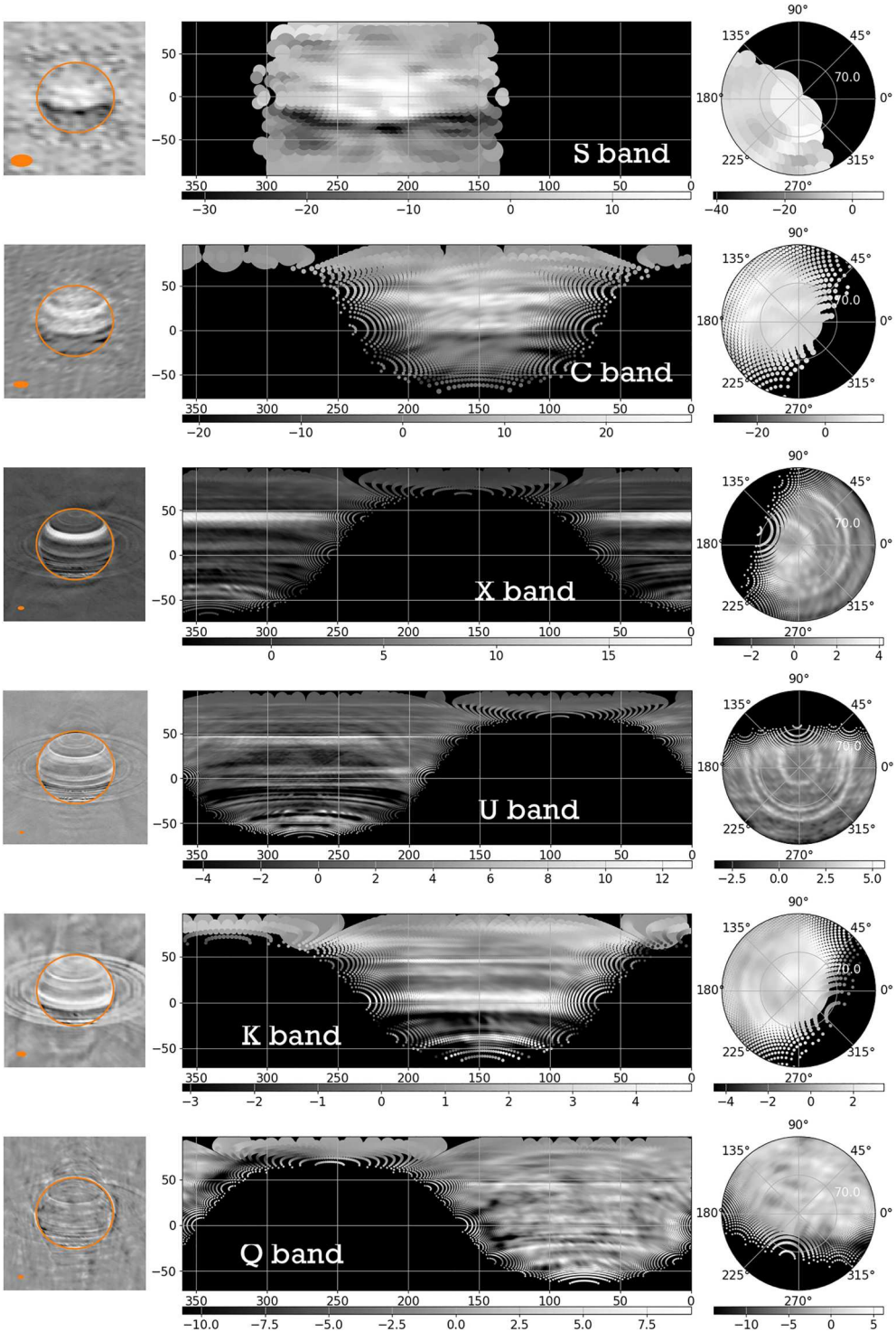

Fig. 2. VLA maps of Saturn in radio bands. (**Left column**) Disk-removed images of Saturn at S, C, X, U, K, and Q bands sequentially from top to bottom. The beam pattern for each band is drawn in the lower left corner of the disk image as ellipses. The orange circle in each panel indicates the limb of the disk. (**Middle column**) Cylindrical projection of the residual brightness temperature. (**Right column**) Polar projection of the residual brightness temperature. The lowest latitude is at 50°N in the projection. These images are rotationally smeared; the center column shows the approximate longitudinal range covered by each observation. A longitude-resolved map for the combined U and X band data was shown in (*48*). B/W color scale shows the residual brightness temperature with a limb-darkened disk subtracted.

bright equator. The dark band in the southern hemisphere is due to the ring occulting the emission of the planet.

The X-band image features an extremely bright latitude band between 40°N and 50°N. The brightness temperature of this latitude band is about 15 K warmer than the neighboring bands, showing that ammonia vapor must be substantially depleted in the atmosphere. Looking at the polar projection map in the right column, we also find a bright ring surrounding the north pole, which we attribute to the deep signature of Saturn′s hexagon, although the hexagonal shape is unclear at the resolution of this image.

The highest spatial resolution is achieved in the U-band images, in which the bright 40°N and 50°N band breaks into two distant narrow bands with one at 40°N and the other at 44°N. This dual-band structure is only present in the U-band images and is realistic as it consistently shows up at all longitudes in the cylindrical projection map. The bright ring–like structure surrounding the pole near 78°N now takes a hexagonal shape in the U-band image. Since its position is colocated with the visible image of the hexagon, we interpret it as being the deep root of Saturn′s polar hexagon. At a higher altitude (~100 mbar), the Cassini/CIRS instrument found warmer temperatures (~4 K) than the neighboring latitudes (*27*). This pattern resembles our finding at the U band. Although the altitude probed by Cassini/CIRS is higher than in our radio map, it is likely that the hexagonal jet remains warm in temperature and extends deep (at least ~2 bars) into the lower troposphere.

The 44°N bright feature in the U-band image also exists in the K-band image, but the 40°N bright feature disappeared, probably due to a decrease in spatial resolution. The bright equatorial zone is the most prominent feature in the K-band image, accompanied by a broad dark band centered near 20°N. The Q-band image is noisy and the banded structure is almost indistinguishable, although at these frequencies we probe similar pressure levels to that of the U band.

Zonal-mean residual emission

Figure 3 shows the zonal-mean latitudinal scans of the radio emission across spectral bands, after a limb-darkened disk was subtracted from each image (Fig. 2). The noises are illustrated as gray ticks in each band. Since the emission angle changes substantially across the disk, we average over 60° in longitude around the central meridian of the disk image. For the S band, we increase the width of the latitude bin to obtain at least eight pixels to have a robust estimate of the noise. Thus, the uncertainty reflects the noise in the radio map, which is much smaller than the calibration uncertainty. Any longitudinally dependent features are smeared out because these scans are zonally averaged. But since these scans cover several spectral bands, they reveal changes in brightness temperatures over a range of altitudes.

These zonal-mean scans at the different wavelengths form, in essence, a spectral data cube; we evaluate these at the emission angle between the local zenith and an Earth′s observer. Multiple bright features, such as the 40°N and 44°N bands, are discernible from the spectral scans and can be correlated across spectral space from top to bottom. In general, a feature appears bright (high brightness temperature) when the ammonia vapor, the main microwave absorber, is depleted compared to the average, or the temperature is high. For example, the brightness temperatures are higher at 45°N in the Q, K, U, and X bands but lower than average in the C band compared to the neighboring latitudes, suggesting two end-member scenarios: (i) The ammonia concentration is depleted at higher altitudes (sensed by Q, K, U, and X bands) and enriched at lower altitudes (sensed by C band), or (ii) the temperature is higher at higher altitudes and lower at lower altitudes compared to the neighboring latitudes. The VLA observation alone cannot resolve the ambiguity, but these two scenarios are always related: Evaporation/sublimation of ammonia rain droplets/ice crystals would simultaneously cool the atmospheric temperature and enrich the ammonia vapor concentration.

To have a quantitative assessment of the physical properties of Saturn′s atmosphere, we perform a beam deconvolution followed by a differential spectral inversion to recover the ammonia concentration anomaly (see Materials and Methods). Fitting the brightness temperature anomaly rather than its absolute value bypasses the 3 to 5% (*28*) calibration uncertainty and leverages the precision of the measurements. Figure 4 shows the deconvolved spectral scans in orange lines and the width of the Gaussian beam in red bars. Deconvolution has the largest effects on K and U band data due to the

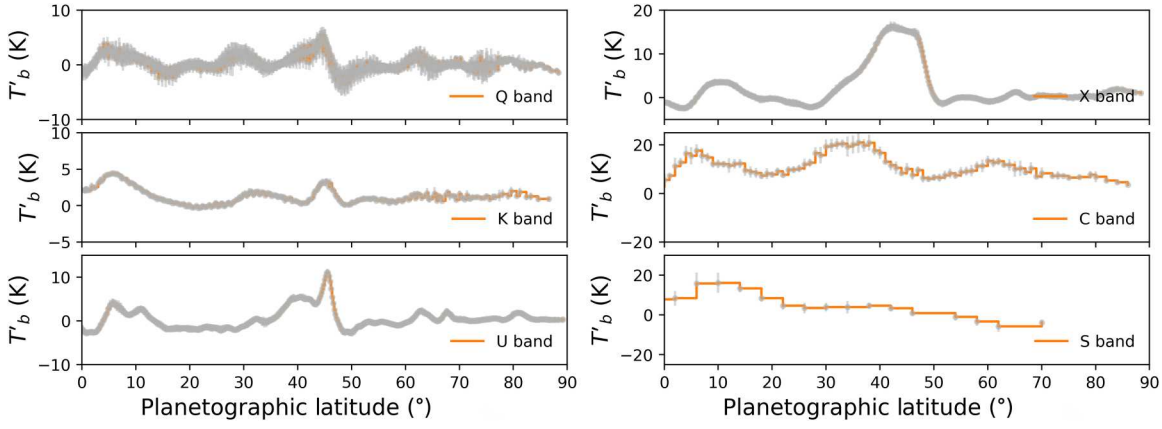

Fig. 3. Residual zonal-mean brightness temperatures at six bands. The mean is obtained by averaging over 60° in longitude around the central meridian of the observed disk. Gray ticks in each panel reflect the 1σ uncertainty estimates from all longitudes within each latitude bin. The spacing of the step segment represents the pixel size of the disk image.

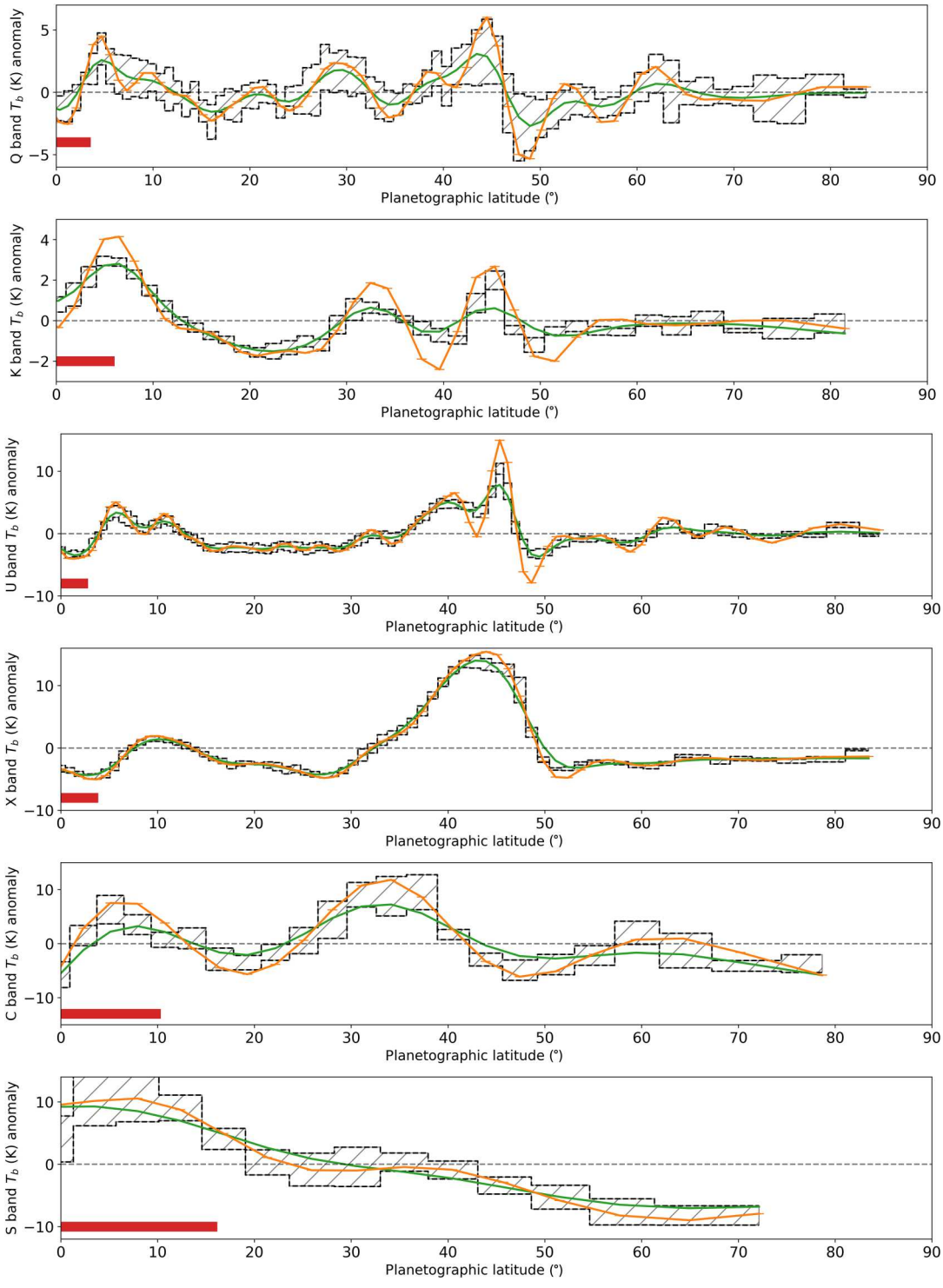

Fig. 4. Deconvolved brightness temperature anomaly. From (**top**) to (**bottom**), the radio bands are ordered as Q, K, U, X, C, and S. Orange lines show the deconvolved brightness temperature anomaly. Cross-hatched patterns indicate the noise level in a latitude bin. Green lines are reconvolved brightness temperature anomalies using the red lines for each band. Red bars at the lower left corner show the FWHM of the Gaussian beam. Anomaly is with respect to the mean emission of the northern hemisphere.

high precision, small beam width, and large spatial variation of the brightness temperatures. After the deconvolution, the peak amplitude of the brightness temperature anomaly is raised and the phase (position of the brightness temperature peaks) of the spectrum is shifted. Deconvolution has a relatively small effect on Q, X, C, and S bands given their relatively smooth variation and/or large beam size.

The variation of the brightness temperatures in Fig. 4 reflects the variability of Saturn's atmospheric composition or temperature on top of an imprecisely determined baseline. From Fig. 1, we find that the brightness temperatures of a homogeneous isentropic model atmosphere could adequately explain the disk-averaged brightness temperatures of Saturn. Therefore, we choose the baseline model of the differential fitting to be the simple homogeneous isentropic model. This choice also provides an additional benefit such that the anomaly map can be compared both vertically (altitude) and horizontally (latitude) since the baseline model has a uniform distribution of ammonia and is isentropic. We further fix the temperature profile and only examine the distribution of ammonia because the observed brightness temperature anomaly is far greater than the increase in temperature due to the giant storm in 2010 (2.4 K) (*29*) or the latitudinal variability of temperature at the 0.5-bar pressure level (~2 K) measured by the Cassini/CIRS instrument (*30*) based on the collision-induced continuum absorption of hydrogen at far infrared. The Cassini/Visible and Infrared Mapping Spectrometer instrument provides somewhat deeper observation of thermal emission at near infrared, but deriving the meridional variability of temperature is impossible because of the degeneracy with PH_3 and aerosols (*31*). The formula and details of the differential fitting are provided in Materials and Methods.

Anomalous ammonia concentration map

Figure 5 shows the ammonia anomaly map with Saturn's zonal wind profile in System III (*32*) for comparison. We find three distinct patches of ammonia anomalies, between 0°N and 12°N, between 25°N and 45°N, and between 55°N and 72°N. There are six occurrences of giant storms on Saturn in the past 150 years: the 1876, 1933, and 1990 storms erupted between 0°N and 12°N; the 1903 and 2010 storms erupted between 35°N and 42°N; and the 1960 storm erupted near 58°N. We find ammonia anomaly signatures for all mid-latitude eruptions and an equatorial mixture with their long-time evolution. Specifically, we find that the ammonia anomaly propagates meridionally in the increasing direction of the zonal wind, meaning that the meridional velocity is associated with the vorticity of the flow. The propagation of the ammonia anomaly is usually stopped at the position of another zonal jet. On the basis of these observations, we suspect that there could be another storm that has occurred near 70°N latitude that was before 1876, the first recorded storm.

Another finding is a division between atmospheric layers at ~3 to 5 bars caused by the giant storms: At altitudes above 3 to 5 bars, the ammonia vapor is depleted, and below that level, the ammonia abundance is enriched. During the eruption of the 2010 storm, the Cassini/Radar observed highly depleted ammonia gas at roughly the 1- to 2-bar level (*12*). But where did the ammonia vapor go? If ammonia is hidden within the ammonia-rich precipitation (*14*), it would reevaporate and enrich the ammonia concentration in the deep atmosphere. This is exactly what we have seen using longer-wavelength radio observations: After a giant storm, ammonia gas is indeed transported from the upper atmosphere to deeper layers. The layering of the atmosphere indicates stable stratification, and the simplest form is that the atmosphere is divided into two distinct layers. On the basis of the observation of the layering, we estimate

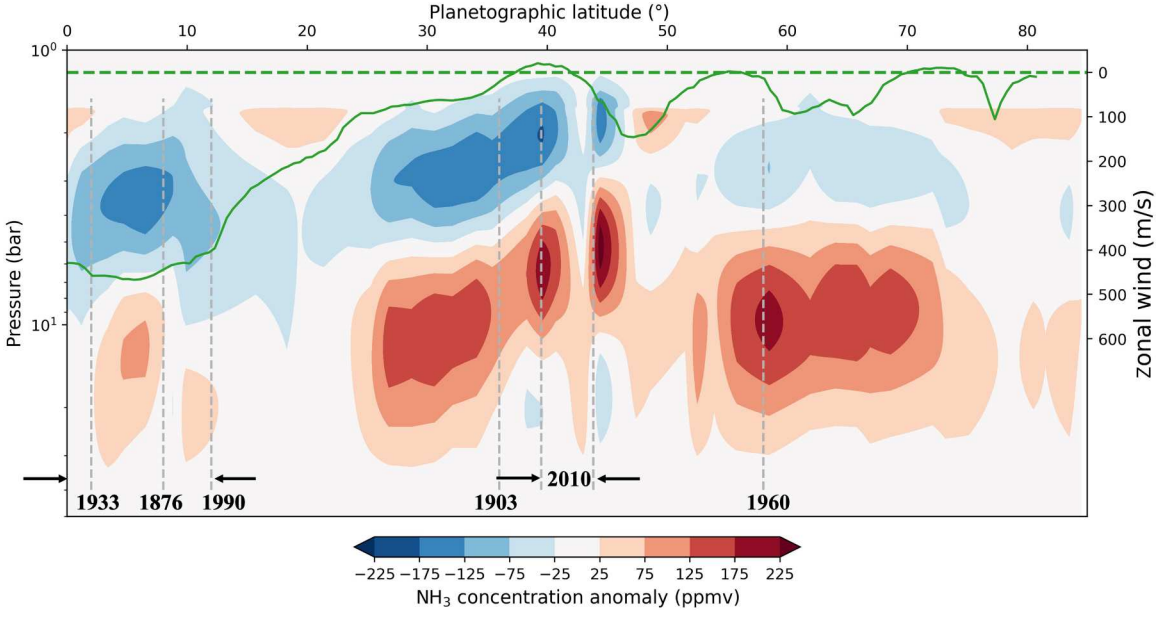

Fig. 5. Ammonia vapor concentration anomaly with respect to a homogeneous model. The zonal wind profile is indicated by the green curve at the top, with its scale along the right *y* axis. The locations and the years of the previous giant storms are annotated in the figure. Storms in 1876, 1933, 1903, and 1960 are denoted by their center locations. The equatorial storms (1876, 1933, and 1990) (*49*) and the 2010 storm (*3–5*) are displayed as a latitude range.

the convective mass flux of the 2010 storm using an energy balance calculation.

The last 2010 giant storm increased Saturn's emitted power in the stormy band by ~9.2%, which translates into a 2.4 K increase in physical temperature (*29*). From the ammonia anomaly map, we find that the transition pressure level is at about $p_b \sim 3$ bars. Therefore, we posit that at least 3 bars of atmospheric mass is warmed up either by the direct thermodynamic response to the latent heat release or by secondary circulation such as the compensating subsidence through adiabatic heating (*6*). The amount of latent heat released per unit area per unit time is equivalent to the product of the mass flux of the upward motion and the mass mixing ratio of water, multiplied by the latent heat of water. Equating that to the increase of column temperature yields

$$c_p \Delta T \frac{p_b S}{g} = L \dot{m}_u q_w S t \quad (1)$$

where the heat capacity of the hydrogen-helium atmosphere is $c_p = 1.3 \times 10^4$ J/(kg K); the increase in temperature is $\Delta T = 2.4$ K. The upward convective mass flux is denoted as $\dot{m}_u$. The spatial area covered by the storm is $S = 3 \times 10^{15}$ m^2 based on the 300,000 km circumference of the planet and the 10,000 km width in latitude, and $t = 6$ months is the duration of the storm. Saturn's gravity at 40°N is $g = 11$ m/s^2. The latent heat of water is $L = 2.5 \times 10^6$ J/kg, and the mass mixing ratio of water participating in the convection is q_w. If we use the deep water mixing ratio, which is about 10% of the total atmospheric mass (*6*), the convective mass flux is

$$\dot{m}_u = \frac{c_p \Delta T p_b}{q_w g t L} = 2.2 \times 10^{-4} \text{ kg/(m}^2\text{s)} \quad (2)$$

Assuming that the detrainment level of the upward convective mass flux occupies one scale height at the physical temperature of 100 K, $H = RT/g = 34$ km, where the atmospheric pressure is $p = 0.4$ bar and the atmosphere density is $\rho = p/(RT) = 0.1$ kg/m^3. The associated cloud expansion rate of the giant storm in 2010 is thus

$$\dot{A} = \frac{\dot{m}_u S}{\rho H} = 1.9 \times 10^2 \text{ km}^2/\text{s} \quad (3)$$

This value is very close to the measured cloud expansion rate of $\dot{A} = 200$ km^2/s based on the sequence of cloud images over the whole lifetime of the storm (*3*, *4*). The division levels of other storms are located at lower altitudes than that of the 2010 storm, indicating potential subsidence over the years following a giant storm. The subsidence could be driven by radiative cooling and convective adjustment. For example, the downward propagation of a stable interface separating a convective interior and a stable upper atmosphere was simulated by a one-dimensional convective adjustment model (*6*). In addition, as described in the theory, the downward propagation is stopped at the water condensation level, which is around 20 bars assuming a 10 times solar water abundance.

The third finding revealed by the ammonia anomaly map is that a mixing barrier seems to form where the zonal wind velocity crosses zero. This is most evident near the two zero-crossings of the zonal wind profile flanking the 40°N westward jet. Specifically, the post-eruption evolution of the 2010 storm is intriguingly split into two distinct components. The northern one propagates northward and the southern one propagates southward, leaving a gap in between.

The gap is located at 43 ± 0.4°N based on the high-resolution U-band image of Saturn. The location is very close to the zero-velocity crossing at 41.8°N using the System III rotation period (10 hours, 39 min, 24 s) determined by Voyager's measurement of Saturn's kilometric radiation in 1978 (*32*). Saturn's rotational period is uncertain because Saturn's dipole magnetic field is not tilted relative to its rotation axis (*33*). Other indirect measurements based on atmospheric dynamics, response to gravity, and ring seismology generally place Saturn's rotation period in between 10 hours 32 min 35 s and 10 hours 34 min 13 s (*34*–*36*), which corresponds to a zero-crossing latitude near 44.2°N. It is unknown what causes the separation and the formation of the gap. We raise a conjecture that the gap could indicate where the zonal wind is zero. This can be tested by a numerical model studying the long-term evolution of the post-eruption tropospheric dynamics.

DISCUSSION

For most of the time, Saturn's atmosphere looks hazy and featureless to the naked eye in contrast to Jupiter's colorful and vibrant atmosphere. This picture changes when we look at Saturn using a radio eye. Despite bland looking at the visible wavelengths, different latitudes on Saturn show dramatic contrast in the radio emission. In 2015, we found substantial brightness temperature variations—greater than the temperature increase caused by the 2010 storm—as a function of latitude and radio wavelength based on spatially resolved radio images of Saturn, as obtained from the VLA. Via a spectral inversion study, we created a latitude-altitude map of ammonia concentration anomalies from these images and correlate the anomalies to the occurrences of past giant storms in the northern hemisphere. The equatorial mixture of storms and storms at mid-latitudes are featured by a depletion of ammonia at altitudes above the 3- to 5-bar level and an enrichment of ammonia below that pressure level. The most likely scenario is that ammonia is transported from the upper atmosphere to the lower atmosphere via precipitation and reevaporation. The ammonia concentration anomaly also seems to propagate meridionally across latitudes during long-term post-eruption evolution. Specifically, the past 2010 storm is divided into two distinct components, with one propagating southward and the other northward, leaving a gap at 43°N. These findings call for more investigations into the large-scale atmospheric dynamics during the post-eruption state of Saturn's atmosphere. Our result shows that Saturn's tropospheric dynamics may be substantially different from Jupiter's. The Juno microwave radiometer revealed a correlation of brightness temperature anomaly with zones and belts. However, on Saturn, the brightness temperature anomalies at radio wavelengths are dominated by giant storms.

The observation we took in 2015 was unable to view Saturn's southern hemisphere due to its rings. We are looking forward to another observing opportunity in 2025 when Saturn's rings will be viewed edge-on and both hemispheres can be observed from Earth. Since there are no detections of giant storms in the southern hemisphere, we expect that brightness temperature variations are smaller in the southern hemisphere than in the north.

MATERIALS AND METHODS

VLA data acquisition and calibration

The VLA data were acquired in January and May 2015 and presented previously with the analysis of Saturn's ring system, referred to here as Zhang *et al.* (*18*). As discussed in Zhang *et al.* (*18*), all data were initially processed and calibrated using the internal VLA calibration pipeline. They subsequently used the MIRIAD software to self-calibrate, clean, and map the data (*19*). Zhang *et al.* (*18*) combined all eight channels in each spectral window, as well as several spectral windows to increase the signal-to-noise ratio (SNR). In U and X bands, the final bandwidth per window was 1 GHz; in the K band, it was 4 GHz; in the Q band, all windows were combined with a resulting bandwidth of almost 8 GHz. In C and S bands, all spectral windows were combined as well, resulting in a bandwidth of 0.25 GHz in each band. For X and U bands, data were obtained in two different array configurations. To increase the sensitivity for atmospheric study, we combined the data obtained on different dates by scaling the flux density of the source to match both observations. This flux density is integrated over the solid angle extended by the radio source, and thus captures the changes in the change of Saturn's diameters on different dates.

The flux density scale was calibrated on the radio source 3C286, with the standard VLA flux calibrator scale (*28*, *37*). The radio source J1558-1409 was used as the complex gain calibrator (phases). Internal and absolute uncertainties in the flux densities are believed to be better than ~3% at most frequencies and 5% at K and Q bands. We adopt these, somewhat conservative, uncertainties in our work during the fit to the disk-averaged brightness temperatures. These uncertainties only affect the precision of the baseline inversion and do not affect the accuracy of the retrieved ammonia anomalies through the differential spectral inversion.

Zhang *et al.* (*18*) used a "planet + ring" model to self-calibrate the data and determine the best-fit parameters for both the planet and Saturn's rings. The planet's brightness temperature T_b of the unocculted portion of the planet's disk was modeled as $T_b = T_0 + T_1\langle\mu_p\rangle$, where T_0 and T_1 are model parameters of the uniform and limb-darkened disk, respectively, and μ_p is the cosine of the emission angle. The rings were modeled using the Simrings code (*38*). Modeling the rings this way enabled Zhang *et al.* (*18*) to determine the ring properties of Saturn's main rings, as, e.g., their optical depth, particle size distribution, composition, and porosity. In our work, we use final calibrated *UV* data from Zhang *et al.* (*18*) and subtract the model for the rings to construct the best possible data for Saturn's atmosphere. Rather than using the combined C&B and B&A array configurations for the X and U data, we instead focus on only the B&A configuration for these bands, although we use the more compact array to calibrate the flux densities.

On the basis of Zhang *et al.*'s model (*18*) fits of Saturn's disk, we determined the disk-averaged brightness temperatures in each spectral window, as summarized in table S1. Since Saturn blocks out the cosmic background radiation (CMB), and the flux density is measured relative to the background, we add the temperature corresponding to the CMB to the disk-averaged brightness temperature. We further used a disk-averaged value of 0.667 for the cosine of the emission angle of the disk when combining the T_0 and T_1 temperatures into a disk-averaged value. While we derive here (table S1) the disk-averaged brightness temperature in each spectral window, to increase the SNR in the maps, we combined all spectral windows per frequency band, resulting in a total of six maps.

Deconvolution algorithm

All radio maps presented here have different resolutions, i.e., they are all "smoothed" by their respective beams, which differ from wavelength to wavelength. To obtain a quantitative assessment of the physical properties of Saturn's atmosphere, we need to convolve models of Saturn's atmosphere with their respective beams in an iterative process to determine the cause of observed variations in brightness temperature with latitude. To speed up this process and to mitigate the effect of the beam picking up cold sky signals when close to the limb, we instead deconvolve the latitudinal scans in each wavelength band and then use a differential spectral inversion to obtain an ammonia anomaly map, i.e., the difference in ammonia profiles relative to the nominal (200 ppm) value as a function of latitude that best matches the data.

We denote the beam-convolved zonal-mean brightness temperature anomaly as $\tilde{T}_b(x)$, where x is the projected distance normal to the observer's line of sight, referred to as the sky coordinate. The corresponding point-wise brightness temperatures are denoted as $T_b(y)$. We approximate the VLA beam pattern as a Gaussian function, denoted as $G(y; s)$, where s represents the full width at half maximum (FWHM) of the beam and is related to the SD of the Gaussian function by $s = 2\sqrt{2\ln 2}\sigma$. Using the sky coordinate x, the beam convolution gives

$$\tilde{T}_b(x) = \int_{-\infty}^{+\infty} T_b(y)G(x-y;s)dy \tag{4}$$

To deconvolve the observed brightness temperature, we use the Fourier transform and regularized optimization. The Fourier transform of Eq. 4 is

$$\mathcal{F}\{\tilde{T}_b\}(w) = \mathcal{F}\{T_b\}(w)\cdot\mathcal{F}\{G\}(w) \tag{5}$$

where w is the angular frequency and the product is performed element-wise at each frequency.

In principle, one can just divide the Fourier transform of the convolved beam, $\mathcal{F}\{\tilde{T}_b\}$, by the Fourier transform of the Gaussian beam, $\mathcal{F}\{G\}(w_i)$, to get the Fourier transform of the pointwise brightness temperature, $\mathcal{F}\{T_b\}(w_i)$, and then invert it for the pointwise brightness temperature. However, this method suffers from numerical instabilities for high-resolution maps. On the one hand, high-resolution observations contain more information, but on the other hand, it introduces more Fourier modes to invert. Usually, the increase of the information content is not enough to constrain the additional Fourier modes, and therefore, a direct division yields an unstable solution. We use regularized optimization to overcome the difficulty. In discretized frequency domain, w_i, Eq. 5 becomes

$$\mathcal{F}\{\tilde{T}_b\}(w_i) = \mathcal{F}\{T_b\}(w_i)\cdot\mathcal{F}\{G\}(w_i), i = 0...n \tag{6}$$

Now, we cast the equation above into a matrix multiplication form such that

$$\mathcal{F}\{\tilde{T}_b\}(w_i) = G_{ij}\cdot\mathcal{F}\{T_b\}(w_j) \tag{7}$$

where $G_{ij} = \mathcal{F}\{G\}(w_i)\delta_{ij}$ are the coefficients of a diagonal matrix. Instead of solving Eq. 7 exactly, we try to obtain a regularized

least-square solution that demands vanishing amplitude for high-frequency modes such that

$$G_{ij} \cdot \mathcal{F}\{T_b\}(w_j) \approx \mathcal{F}\{\tilde{T}_b\}(w_i) \tag{8}$$

subject to small $\mathcal{F}\{T_b\}(w_j)$ for large w_j. The way to do it is to add a penalty term for the amplitude of $\mathcal{F}\{T_b\}(w_j)$ as a function of its w_j. By doing experiments with triangle functions (see the Supplementary Materials, section B), we find that a penalty proportional to frequency squared works well for the deconvolution. Mathematically, the cost function of the minimization is

$$\begin{aligned}\text{Cost function} &= \chi^2 + \lambda^2 \sum_{i=0}^{n-1} [w_i \mathcal{F}\{T_b\}(w_i)]^2 \\ &= \sum_{i=0}^{n-1} [G_{ij} \cdot \mathcal{F}\{T_b\}(w_j) - \mathcal{F}\{\tilde{T}_b\}(w_i)]^2 \\ &\quad + \lambda^2 \sum_{i=0}^{n-1} [w_i \mathcal{F}\{T_b\}(w_i)]^2\end{aligned} \tag{9}$$

where λ is a tunable parameter governing the strength of the regularization. Written in matrix notation, the least-square solution to Eq. 9 is

$$F\{\mathbf{T_b}\} = (\mathbf{G}^T\mathbf{G} + \lambda^2 \mathbf{W}^T\mathbf{W})^{-1}\mathbf{G}^T F\{\tilde{\mathbf{T}}_\mathbf{b}\} \tag{10}$$

where W is a diagonal matrix with its elements being $W_{ij} = w_i\delta_{ij}$. The component form of Eq. 10 is

$$\mathcal{F}\{T_b\}(w_i) = \frac{\mathcal{F}\{G\}(w_i)}{\mathcal{F}\{G\}(w_i)^2 + \lambda^2 w_i^2} \mathcal{F}\{\tilde{T}_b\}(w_i) \tag{11}$$

Compared to Eq. 6, the λ^2 term in the denominator of Eq. 11 provides the stability of the solution. For low-frequency modes, where $\mathcal{F}\{G\}(w) \gg \lambda^2 w^2$, Eq. 11 reduces to Eq. 6. For high-frequency modes, their amplitude would decay as w^{-2}. The cutoff frequency, w_c, occurs at $\mathcal{F}\{G\}(w_c) = \lambda w_c$. It is useful to define a cutoff wavelength, $L_c = \frac{2\pi}{w_c}$, to denote the spatial resolution that can be recovered from the deconvolution. Spatial variations at wavelength smaller than L_c will be suppressed by the deconvolution, and variations greater than L_c will be preserved. Note that Eq. 11 bears resemblance to the Wiener deconvolution, which has been used extensively in the imaging processing community to sharpen a noisy image (*39*), such as restoring the Hubble Space Telescope (HST) images (*40*). However, the primary goal of the Wiener deconvolution is to clean up a distorted image due to random noise, and our goal is to recover the underlying pointwise brightness temperature from a (beam-convolved) observation. For a Gaussian-shaped beam, its Fourier transform is

$$\begin{aligned}\mathcal{F}\{G\}(w;\sigma) &= \int_{-\infty}^{+\infty} \frac{1}{\sqrt{2\pi}\sigma} \exp\left(-\frac{x^2}{2\sigma^2}\right) \exp(-iwx) dx \\ &= \exp\left(-\frac{1}{2}\sigma^2 w^2\right)\end{aligned} \tag{12}$$

We calculate the discrete Fourier transform of the convolved brightness temperature, $\mathcal{F}\{\tilde{T}_b\}$, using fast Fourier transform (FFT) at discrete frequencies w_i. Then, we use Eq. 12 to calculate the Fourier transform of a Gaussian beam at the same discrete frequencies and apply the result to Eq. 11 to get the spectral amplitudes of the pointwise brightness temperature. Last, inverse FFT is performed to recover the deconvolved brightness temperatures.

To examine the performance of the deconvolution, we reconvolve the beam using Eq. 5 and compare that to the original (beam-convolved) brightness temperatures. The results are displayed in fig. S2. The choice of the penalty strength λ^2 depends on the desired cutoff wavelength L_c, which is related to the width of the radio beam. From the synthetic study of a triangle signal function (Supplementary Materials, section B), we conclude that the spatial sampling resolution can be between one-quarter and one-half of the beam's FWHM. For S, C, and X bands, we use one-half of the beam's FWHM as the cutoff wavelength, and for U, K, and Q bands, we use one-quarter of the beam's FWHM as the cutoff wavelength. The effect of cutoff wavelength can be illustrated by looking at the distribution of the Fourier amplitudes. For example, fig. S2 shows the real part and the imaginary part of the Fourier amplitudes of the beam-convolved brightness temperatures (blue circles and blue crosses). The cutoff wavelength of the S-band data is visually identified at L_c = 0.1 L, where L is the diameter of Saturn's disk, and that for the X band decreases to about 0.02 L. The beam's FWHM at the S band is about 1/5 L, and therefore, any variations of wavelength smaller than 1/10 L are suppressed. Deconvolution does not have an effect over wavelengths greater than 1/10 L. Large-scale (compared to the beam width) features are preserved in the deconvolution.

Differential spectral inversion method

After the deconvolution, we perform a differential fitting using the algorithm below. Let $T_b(y, \mu; \lambda)$ be the brightness temperature at latitude y, at cosine emission angle $\mu = \cos\theta$, and at wavelength λ. We decompose T_b into a baseline component T_b^0 subject to a calibration uncertainty and a fluctuation component T_b^1 subject to a measurement precision such that

$$T_b(y;\mu,\lambda) = T_b^0(\mu_0,\lambda) + \varepsilon(\lambda) + T_b^1(y;\mu,\lambda) + \delta(y,\lambda) \tag{13}$$

where μ_0 is the averaged emission angle, $\varepsilon(\lambda)$ is the random variable representing the calibration uncertainty as a function of wavelength only, and $\delta(y, \lambda)$ is the random variable representing the measurement precision, which is a function of both wavelength and latitude. We assume that $T_b^0 \gg T_b^1$ and the calibration uncertainty is much larger than the precision of the measurement: $\varepsilon \gg \delta$. To represent the fluctuation, we request the average of T_b^1 to be zero. Therefore, $T_b^0 + \varepsilon$ can be obtained by spatial average and $T_b^1 + \delta$ is the residual after subtracting the mean.

Suppose that the radiative transfer equation is written as

$$T_b(y;\mu,\lambda) = f[q(y);\mu,\lambda] \tag{14}$$

where q represents the vertical profile of ammonia vapor, which is a function of latitude. Suppose that there exists an unknown profile, $\hat{q}$, satisfying

$$f(\hat{q};\mu,\lambda) = T_b^0(\mu_0,\lambda) + \varepsilon(\lambda) \tag{15}$$

we use the mean value theorem to obtain

$$T_b(y;\mu,\lambda) = f(\hat{q};\mu,\lambda) + f'[q_a(y);\mu,\lambda][q(y) - \hat{q}] \tag{16}$$

where $q_a(y)$ is between $q(y)$ and $\hat{q}$. Upon matching the terms in Eqs.

13, 15, and 16, we find that

$$f'[q_a(y);\mu,\lambda][q(y)-\hat{q}] = T_b^1(y;\mu,\lambda)+\delta(y,\lambda) \quad (17)$$

On the other hand, if Eq. 15 can be approximately fitted by a known profile, q_0, within the calibration uncertainty such that

$$f(q_0;\mu,\lambda) \approx T_b^0(\mu_0,\lambda)+\varepsilon(\lambda) \quad (18)$$

Then, for any profile $q(y)$, using the mean value theorem again, we have

$$f(q(y);\mu,\lambda) = f(q_0;\mu,\lambda)+f'[q_b(y);\mu,\lambda][q(y)-q_0] \quad (19)$$

where q_b is between q_0 and $q(y)$. Note that q_b may not be known, but $f'(q_b)$ can be precisely evaluated from the radiative transfer calculation. Subtracting Eq. 19 from Eq. 17 yields

$$f'[q_a(y);\mu,\lambda][q(y)-\hat{q}] - f'[q_b(y);\mu,\lambda][q(y)-q_0] =$$

$$T_b^1(y;\mu,\lambda) - \{f[q(y);\mu,\lambda]-f[q_0;\mu,\lambda]\}+\delta(y,\lambda) \quad (20)$$

Since q_0 and $\hat{q}$ are sufficiently close (up to the calibration uncertainty) and if the brightness temperature function $f(q)$ is approximately linear for a range of q that yields small variation of T_b^1 compared to T_b^0, we can safely assume that

$$f'[q_a(y);\mu,\lambda] = f'[q_b(y);\mu,\lambda] \quad (21)$$

without knowing $\hat{q}$ and q_a exactly. Denote the ammonia concentration anomalies as

$$\delta^M q = q(y)-q_0 \quad (22)$$

$$\delta^A q = q(y)-\hat{q} \quad (23)$$

the differential fitting formula reads as

$$f'[q_b(y);\mu,\lambda](\delta^A q-\delta^M q) = T_b^1(y;\mu,\lambda) - \{f[q(y);\mu,\lambda] - f[q_0;\mu,\lambda]\}+\delta(y,\lambda) \quad (24)$$

and the minimization function is

$$\text{Minimize}_q \left|T_b^1(y;\mu,\lambda) - \{f[q(y);\mu,\lambda]-f[q_0;\mu,\lambda]\}\right|^2/\delta(y,\lambda)^2 \quad (25)$$

If Eq. 21 is strictly valid, then the fitted ammonia anomaly $\delta^M q$ converges to the true ammonia anomaly $\delta^A q$. Otherwise, the inference would be biased. The validity of Eq. 21 depends on how close q_0 is to $\hat{q}$ and how linear the brightness temperature function is with respect to the ammonia concentration. Figure S7 shows the optical depths across various VLA radio bands. It shows that different bands are sensitive to different pressure levels. At about 10 bars, S band's optical depth is close to 1. At about 20 bars, S band's optical depth increases to 4. Linearity is best observed when the optical depth is close to 1. We terminate our inversion algorithm at 25 bars, as beyond this point, the sensitivity is lost and the linearity assumption is no longer valid. Nevertheless, using the differential fitting formula, Eq. 25 bypasses the large calibration uncertainty ε and leverages the measurement precision δ.

The fitting and radiative transfer were performed using the Markov chain Monte Carlo (MCMC) method as described in (*24*, *41*). First, we divide the atmosphere into five layers with pressure boundaries at 25, 12.2, 5.98, 2.93, 1.43, and 0.7 bars, respectively. These pressure levels are chosen on the basis of log spacing between 25 and 0.7 bars, which denote the lower and upper boundary of the spectral inversion domain. Second, we fix the ammonia concentration at 200 ppm at 25 bars (see the Supplementary Materials, section A, for the choice) and vary the ammonia concentration at the other pressure levels. The ammonia profiles in between these pressure levels are smoothly interpolated. In total, we have six sampling variables. Third, we calculate the brightness temperatures of this model atmosphere at the emission angle specified by the observing geometry for each frequency band. Last, we minimize Eq. 25 based on the MCMC algorithm. More discussions on the inversion parameters are provided in the Supplementary Materials, section C.

Supplementary Materials

This PDF file includes:

Sections A to C
Figs. S1 to S8
Table S1
References

REFERENCES AND NOTES

1. A. Sanchez-Lavega, E. Battaner, The nature of Saturn's atmospheric great white spots. *Astron. Astrophys.* **185**, 315–326 (1987).
2. A. Sanchez-Lavega, Saturn's great white spots. *J. Nonlinear Sci.* **4**, 341–353 (1994).
3. K. M. Sayanagi, U. A. Dyudina, S. P. Ewald, G. Fischer, A. P. Ingersoll, W. S. Kurth, G. D. Muro, C. C. Porco, R. A. West, Dynamics of Saturn's great storm of 2010–2011 from cassini iss and rpws. *Icarus* **223**, 460–478 (2013).
4. A. Sánchez-Lavega, T. del Río-Gaztelurrutia, R. Hueso, J. M. Gómez-Forrellad, J. F. Sanz-Requena, J. Legarreta, E. García-Melendo, F. Colas, J. Lecacheux, L. N. Fletcher, D. Barrado-Navascués, D. Parker; The International Outer Planet Watch (IOPW) Team, Deep winds beneath Saturn's upper clouds from a seasonal long-lived planetary-scale storm. *Nature* **475**, 71–74 (2011).
5. G. Fischer, W. Kurth, D. Gurnett, P. Zarka, U. Dyudina, A. Ingersoll, S. Ewald, C. Porco, A. Wesley, C. Go, M. Delcroix, A giant thunderstorm on Saturn. *Nature* **475**, 75–77 (2011).
6. C. Li, A. P. Ingersoll, Moist convection in hydrogen atmospheres and the frequency of Saturn's giant storms. *Nat. Geosci.* **8**, 398–403 (2015).
7. L. N. Fletcher, B. Hesman, R. Achterberg, P. Irwin, G. Bjoraker, N. Gorius, J. Hurley, J. Sinclair, G. Orton, J. Legarreta, E. García-Melendo, A. Sánchez-Lavega, P. L. Read, A. A. Simon-Miller, F. M. Flasar, The origin and evolution of Saturn's 2011–2012 stratospheric vortex. *Icarus* **221**, 560–586 (2012).
8. L. N. Fletcher, S. Guerlet, G. S. Orton, R. G. Cosentino, T. Fouchet, P. G. Irwin, L. Li, F. M. Flasar, N. Gorius, R. Morales-Juberías, Disruption of Saturn's quasi-periodic equatorial oscillation by the great northern storm. *Nat. Astron.* **1**, 765–770 (2017).
9. B. Hesman, G. Bjoraker, P. Sada, R. Achterberg, D. Jennings, P. Romani, A. Lunsford, L. Fletcher, R. Boyle, A. Simon-Miller, C. A. Nixon, P. G. J. Irwin, Elusive ethylene detected in Saturn's northern storm region. *Astrophys. J.* **760**, 24 (2012).
10. J. I. Moses, E. S. Armstrong, L. N. Fletcher, A. J. Friedson, P. G. Irwin, J. A. Sinclair, B. E. Hesman, Evolution of stratospheric chemistry in the Saturn storm beacon region. *Icarus* **261**, 149–168 (2015).
11. M. Janssen, A. Ingersoll, M. Allison, S. Gulkis, A. Laraia, K. Baines, S. Edgington, Y. Anderson, K. Kelleher, F. Oyafuso, Saturn's thermal emission at 2.2-cm wavelength as imaged by the cassini radar radiometer. *Icarus* **226**, 522–535 (2013).
12. A. Laraia, A. Ingersoll, M. A. Janssen, S. Gulkis, F. Oyafuso, M. Allison, Analysis of Saturn's thermal emission at 2.2-cm wavelength: Spatial distribution of ammonia vapor. *Icarus* **226**, 641–654 (2013).
13. A. P. Showman, I. de Pater, Dynamical implications of Jupiter's tropospheric ammonia abundance. *Icarus* **174**, 192–204 (2005).
14. T. Guillot, D. J. Stevenson, S. K. Atreya, S. J. Bolton, H. N. Becker, Storms and the depletion of ammonia in Jupiter: I. microphysics of "mushballs". *J. Geophys. Res. Planets* **125**, e2020JE006403 (2020).

15. T. Guillot, C. Li, S. J. Bolton, S. T. Brown, A. P. Ingersoll, M. A. Janssen, S. M. Levin, J. I. Lunine, G. S. Orton, P. G. Steffes, D. J. Stevenson, Storms and the depletion of ammonia in Jupiter: II. Explaining the juno observations. *J. Geophys. Res. Planets* **125**, e2020JE006404 (2020).
16. S. Weidenschilling, J. Lewis, Atmospheric and cloud structures of the jovian planets. *Icarus* **20**, 465–476 (1973).
17. L. Li, B. J. Conrath, P. J. Gierasch, R. K. Achterberg, C. A. Nixon, A. A. Simon-Miller, F. M. Flasar, D. Banfield, K. H. Baines, R. A. West, A. P. Ingersoll, A. R. Vasavada, A. D. del Genio, C. C. Porco, A. A. Mamoutkine, M. E. Segura, G. L. Bjoraker, G. S. Orton, L. N. Fletcher, P. G. J. Irwin, P. L. Read, Saturn's emitted power. *J. Geophys. Res. Planets* **115**, E11002 (2010).
18. Z. Zhang, A. Hayes, I. de Pater, D. Dunn, M. Janssen, P. Nicholson, J. Cuzzi, B. Butler, R. Sault, S. Chatterjee, VLA multi-wavelength microwave observations of Saturn's C and B rings. *Icarus* **317**, 518–548 (2019).
19. M. Wright, R. Sault, Mapping cygnus a at 3 millimeter wavelength with the miriad system. *Astrophys J.* **402**, 546–549 (1993).
20. G. F. Lindal, The atmosphere of Neptune: An analysis of radio occultation data acquired with Voyager 2. *Astron. J.* **103**, 967–982 (1992).
21. M. Asplund, N. Grevesse, A. J. Sauval, P. Scott, The chemical composition of the sun. *Annu. Rev. Astron. Astrophys.* **47**, 481–522 (2009).
22. F. H. Briggs, P. D. Sackett, Radio observations of Saturn as a probe of its atmosphere and cloud structure. *Icarus* **80**, 77–103 (1989).
23. I. de Pater, E. M. Molter, C. M. Moeckel, A review of radio observations of the giant planets: Probing the composition, structure, and dynamics of their deep atmospheres. *Remote Sens.* **15**, 1313 (2023).
24. C. Li, A. Ingersoll, M. Janssen, S. Levin, S. Bolton, V. Adumitroaie, M. Allison, J. Arballo, A. Bellotti, S. Brown, S. Ewald, L. Jewell, S. Misra, G. Orton, F. Oyafuso, P. Steffes, R. Williamson, The distribution of ammonia on Jupiter from a preliminary inversion of juno microwave radiometer data. *Geophys. Res. Lett.* **44**, 5317–5325 (2017).
25. I. de Pater, D. Dunn, P. Romani, K. Zahnle, Reconciling Galileo probe data and ground-based radio observations of ammonia on Jupiter. *Icarus* **149**, 66–78 (2001).
26. C. Moeckel, I. de Pater, D. DeBoer, Ammonia abundance derived from juno mwr and vla observations of Jupiter. *Planet. Sci. J.* **4**, 25 (2023).
27. L. Fletcher, P. Irwin, G. Orton, N. Teanby, R. Achterberg, G. Bjoraker, P. Read, A. Simon-Miller, C. Howett, R. De Kok, N. Bowles, S. B. Calcutt, B. Hesman, F. M. Flasar, Temperature and composition of Saturn's polar hot spots and hexagon. *Science* **319**, 79–81 (2008).
28. R. Perley, K. Meisenheimer, High-fidelity VLA imaging of the radio structure of 3C273. *Astron. Astrophys.* **601**, A35 (2017).
29. L. Li, X. Jiang, H. J. Trammell, Y. Pan, J. Hernandez, B. J. Conrath, P. J. Gierasch, R. K. Achterberg, C. A. Nixon, F. M. Flasar, S. Perez-Hoyos, R. A. West, K. H. Baines, B. Knowles, Saturn's giant storm and global radiant energy. *Geophys. Res. Lett.* **42**, 2144–2148 (2015).
30. L. Fletcher, P. Irwin, N. Teanby, G. Orton, P. Parrish, R. de Kok, C. Howett, S. Calcutt, N. Bowles, F. Taylor, Characterising Saturn's vertical temperature structure from Cassini/CIRS. *Icarus* **189**, 457–478 (2007).
31. L. N. Fletcher, K. H. Baines, T. W. Momary, A. P. Showman, P. G. Irwin, G. S. Orton, M. Roos-Serote, C. Merlet, Saturn's tropospheric composition and clouds from cassini/vims 4.6–5.1μm nightside spectroscopy. *Icarus* **214**, 510–533 (2011).
32. M. D. Desch, M. Kaiser, Voyager measurement of the rotation period of Saturn's magnetic field. *Geophys. Res. Lett.* **8**, 253–256 (1981).
33. M. K. Dougherty, H. Cao, K. K. Khurana, G. J. Hunt, G. Provan, S. Kellock, M. E. Burton, T. A. Burk, E. J. Bunce, S. W. Cowley, M. G. Kivelson, C. T. Russell, D. J. Southwood, Saturn's magnetic field revealed by the cassini grand finale. *Science* **362**, eaat5434 (2018).
34. P. Read, T. Dowling, G. Schubert, Saturn's rotation period from its atmospheric planetary-wave configuration. *Nature* **460**, 608–610 (2009).
35. J. D. Anderson, G. Schubert, Saturn's gravitational field, internal rotation, and interior structure. *Science* **317**, 1384–1387 (2007).
36. C. Mankovich, M. S. Marley, J. J. Fortney, N. Movshovitz, Cassini ring seismology as a probe of Saturn's interior. I. Rigid rotation. *Astrophys J.* **871**, 1 (2019).
37. R. A. Perley, B. J. Butler, An accurate flux density scale from 1 to 50 ghz. *Astrophys. J. Suppl. Ser.* **204**, 19 (2013).
38. D. E. Dunn, L. A. Molnar, J. D. Fix, More microwave observations of Saturn: Modeling the ring with a monte carlo radiative transfer code. *Icarus* **160**, 132–160 (2002).
39. R. Brown, P. Hwang, *Introduction to Random Signals and Applied Kalman Filtering* (John Wiley & Sons Inc., 1992).
40. E. Sekko, G. Thomas, A. Boukrouche, A deconvolution technique using optimal wiener filtering and regularization. *Signal Process.* **72**, 23–32 (1999).
41. C. Li, T. Le, X. Zhang, Y. L. Yung, A high-performance atmospheric radiation package: With applications to the radiative energy budgets of giant planets. *J. Quant. Spectrosc. Radiat. Transf.* **217**, 353–362 (2018).
42. M. Klein, M. Janssen, S. Gulkis, E. Olsen, Saturn's microwave spectrum: Implications for the atmosphere and the rings, in *Its The Saturn System* (NASA, 1978).
43. I. De Pater, J. R. Dickel, Multifrequency radio observations of Saturn at ring inclination angles between 5 and 26 degrees. *Icarus* **94**, 474–492 (1991).
44. F. van der Tak, I. de Pater, A. Silva, R. Millan, Time variability in the radio brightness distribution of Saturn. *Icarus* **142**, 125–147 (1999).
45. J. Weiland, N. Odegard, R. Hill, E. Wollack, G. Hinshaw, M. Greason, N. Jarosik, L. Page, C. Bennett, J. Dunkley, B. Gold, M. Halpern, A. Kogut, E. Komatsu, D. Larson, M. Limon, S. S. Meyer, M. R. Nolta, K. M. Smith, D. N. Spergel, G. S. Tucker, E. L. Wright, Seven-year Wilkinson microwave anisotropy probe (wmap*) observations: Planets and celestial calibration sources. *Astrophys. J. Suppl. Ser.* **192**, 19 (2011).
46. Planck Collaboration, Y. Akrami, M. Ashdown, J. Aumont, C. Baccigalupi, M. Ballardini, A. J. Banday, R. B. Barreiro, N. Bartolo, S. Basak, K. Benabed, J.-P. Bernard, M. Bersanelli, P. Bielewicz, L. Bonavera, J. R. Bond, J. Borrill, F. R. Bouchet, F. Boulanger, M. Bucher, C. Burigana, R. C. Butler, E. Calabrese, J.-F. Cardoso, J. Carron, H. C. Chiang, L. P. L. Colombo, B. Comis, F. Couchot, A. Coulais, B. P. Crill, A. Curto, F. Cuttaia, P. de Bernardis, A. de Rosa, G. de Zotti, J. Delabrouille, E. Di Valentino, C. Dickinson, J. M. Diego, O. Doré, A. Ducout, X. Dupac, F. Elsner, T. A. Enßlin, H. K. Eriksen, E. Falgarone, Y. Fantaye, F. Finelli, M. Frailis, A. A. Fraisse, E. Franceschi, A. Frolov, S. Galeotta, S. Galli, K. Ganga, R. T. Génova-Santos, M. Gerbino, J. González-Nuevo, K. M. Górski, A. Gruppuso, J. E. Gudmundsson, F. K. Hansen, G. Helou, S. Henrot-Versillé, D. Herranz, E. Hivon, A. H. Jaffe, W. C. Jones, E. Keihänen, R. Keskitalo, K. Kiiveri, J. Kim, T. S. Kisner, N. Krachmalnicoff, M. Kunz, H. Kurki-Suonio, G. Lagache, J.-M. Lamarre, A. Lasenby, M. Lattanzi, C. R. Lawrence, M. Le Jeune, E. Lellouch, F. Levrier, M. Liguori, P. B. Lilje, V. Lindholm, M. López-Caniego, Y.-Z. Ma, J. F. Macías-Pérez, G. Maggio, D. Maino, N. Mandolesi, M. Maris, P. G. Martin, E. Martínez-González, S. Matarrese, N. Mauri, J. D. McEwen, A. Melchiorri, A. Mennella, M. Migliaccio, M.-A. Miville-Deschênes, D. Molinari, A. Moneti, L. Montier, R. Moreno, G. Morgante, P. Natoli, C. A. Oxborrow, D. Paoletti, B. Partridge, G. Patanchon, L. Patrizii, O. Perdereau, F. Piacentini, S. Plaszczynski, G. Polenta, J. P. Rachen, B. Racine, M. Reinecke, M. Remazeilles, A. Renzi, G. Rocha, E. Romelli, C. Rosset, G. Roudier, J. A. Rubiño-Martın, B. Ruiz-Granados, L. Salvati, M. Sandri, M. Savelainen, D. Scott, G. Sirri, L. D. Spencer, A.-S. Suur-Uski, J. A. Tauber, D. Tavagnacco, M. Tenti, L. Toffolatti, M. Tomasi, M. Tristram, T. Trombetti, J. Valiviita, F. Van Tent, P. Vielva, F. Villa, I. K. Wehus, A. Zacchei, Planck intermediate results: LII. Planet flux densities. *Astron. Astrophys.* **607**, A122 (2017).
47. M. Maris, E. Romelli, M. Tomasi, A. Gregorio, M. Sandri, S. Galeotta, D. Tavagnacco, M. Frailis, G. Maggio, A. Zacchei, Revised planet brightness temperatures using the Planck/LFI 2018 data release. *Astron. Astrophys.* **647**, A104 (2021).
48. I. de Pater, B. Butler, R. J. Sault, A. Moullet, C. Moeckel, J. Tollefson, K. de Kleer, M. Gurwell, S. Milam, in *Science with a Next Generation Very Large Array*, E. Murphy, Ed. (Astronomical Society of the Pacific, 2018), vol. 517 of Astronomical Society of the Pacific Conference Series, p. 49.
49. A. Sanchez-Lavega, F. Colas, J. Lecacheux, P. Laques, I. Miyazaki, D. Parker, The great white spot and disturbances in Saturn's equatorial atmosphere during 1990. *Nature* **353**, 397–401 (1991).
50. O. Mousis, L. Fletcher, J.-P. Lebreton, P. Wurz, T. Cavalié, A. Coustenis, R. Courtin, D. Gautier, R. Helled, P. G. J. Irwin, A. D. Morse, N. Nettelmann, B. Marty, P. Rousselot, O. Venot, D. H. Atkinson, J. H. Waite, K. R. Reh, A. Simon-Miller, S. Atreya, N. André, M. Blanc, I. A. Daglis, G. Fischer, W. D. Geppert, T. Guillot, M. M. Hedman, R. Hueso, E. Lellouch, J. I. Lunine, C. D. Murray, J. O'Donoghue, M. Rengel, A. Sanchez-Lavega, F.-X. Schmider, A. Spiga, T. Spilker, J.-M. Petit, M. S. Tiscareno, M. Ali-Dib, K. Altwegg, A. Bouquet, C. Briois, T. Fouchet, S. Guerlet, T. Kostiuk, D. Lebleu, R. Moreno, G. S. Orton, J. Poncy, Scientific rationale for Saturn's in situ exploration. *Planet. Space Sci.* **104**, 29–47 (2014).

Acknowledgments: The National Radio Astronomy Observatory (NRAO) is a facility of NSF operated under cooperative agreement by Associated Universities Inc. VLA data used in this report, associated with project code VLA/14B-401, are available from the NRAO Science Data Archive at https://archive.nrao.edu/archive/advquery.jsp. **Funding:** This work is supported by the Heising-Simons Foundation under the 51 Pegasi b fellowship. **Author contributions:** I.d.P., B.B., R.J.S., and Z.Z. performed observation and data reduction (I.d.P. was the principal investigator on the observing proposal). C.L. performed the analysis, including radiative transfer modeling, deconvolution, and differential spectral inversion. I.d.P. and C.M. performed independent radiative transfer modeling to verify the result. C.L., I.d.P., and C.M. wrote the manuscript. D.d. provided the radiobear software for an independent check. **Competing interests:** The authors declare that they have no competing interest. **Data and materials availability:** Raw data are available at https://data.nrao.edu. The computer codes to process the raw data are available at https://casa.nrao.edu, and the Miriad software is available at https://atnf.csiro.au/computing/software/miriad/. The processed images, data, and processing scripts are available at https://github.com/chengcli/2023.SaturnVLA/. The spectral inversion codes are available at https://github.com/david-deboer/radiobear and https://github.com/chengcli/canoe/. A frozen version of the code that performed the inversion is uploaded to the Zenodo archive with DOI:10.5281/zenodo.8117538. The VLA images are uploaded to the Zenodo archive with DOI:10.5281/zenodo.8117555. All data needed to evaluate the conclusions in the paper are present in the paper and/or the Supplementary Materials.

Submitted 31 January 2023
Accepted 12 July 2023

Published 11 August 2023
10.1126/sciadv.adg9419

ScienceAdvances

Long-lasting, deep effect of Saturn's giant storms

Cheng Li, Imke de Pater, Chris Moeckel, R. J. Sault, Bryan Butler, David deBoer, and Zhimeng Zhang

Sci. Adv. **9** (32), eadg9419. DOI: 10.1126/sciadv.adg9419

Science Advances (ISSN 2375-2548) is published by the American Association for the Advancement of Science. 1200 New York Avenue NW, Washington, DC 20005. The title *Science Advances* is a registered trademark of AAAS.